Title

Engineering Surface Oxygenated Functionalities on Commercial Carbon toward Ultrafast Sodium Storage in Ether-Based Electrolytes

Journal

ACS Applied Materials & Interfaces, 12(33)

ISSN

1944-8244

Authors

Xiao, Wei

Sun, Qian

Liu, Jian

et al.

Publication Date

2020-08-19

DOI

10.1021/acsami.0c08899

Surface Oxygenated Functionalities Enabled Fast Sodium Storage for Carbon Anode Material in Ether-based Electrolyte

Wei Xiao[1,2,4], Qian Sun[1], Jian Liu[1], Biwei Xiao[1], Xia Li[1], Per-Anders Glans[3], Jun Li[2], Ruying Li[1], Xifei Li[4], Jinghua Guo[3], Wanli Yang[3], Tsun-Kong Sham[2*], Xueliang Sun[1*]

1. Department of Mechanical & Materials Engineering, University of Western Ontario, London, Ontario, N6A 5B9, Canada

2. Department of Chemistry, University of Western Ontario, London, Ontario, N6A 5B7, Canada

3. Advanced Light Source, Lawrence Berkeley National Laboratory, Berkeley, California, 94720, United States

4. Institute of Advanced Electrochemical Energy, School of Materials Science and Engineering, Xi'an University of Technology, Xi'an, Shaanxi, 710048, China

Abstract:

The pursuit of a high-capacity anode material has been urgently required for commercializing sodium-ion batteries with a high energy density and an improved safety. In the absence of the thermodynamically stable sodium intercalated compounds with graphite, constructing nanostructures with expanded interlayer distances is still the mainstream of developing high-performance carbonaceous anodes. In this regard, a porous carbon material has been fabricated by a facile CO_2 thermal etching process and the great importance of oxygenated functionalities for sodium ion storage is firstly uncovered by the electrochemical and physiochemical characterizations. Due to the abundant ionic/electronic pathways and more active sodium storage sites in microporous structure with the noticeable pseudocapacitive behaviors, the functionalized porous carbon could achieve a highly reversible capacity of 505 mAh g^{-1} at 50 mA g^{-1}, an excellent rate performance of 181 mAh g^{-1} at 16000 mA g^{-1}, and an exceptional rate cycle stability of 176 mAh g^{-1} at 3200 mA g^{-1} over 1000 cycles. These outstanding electrochemical performances should be attributed to a synergistic mechanism, fully utilizing the graphitic and amorphous structures for the simultaneous intercalations of sodium ions and solvated sodium ion species, respectively. Additionally, the controllable formation and evolution of a robust but thin solid electrolyte interphase (SEI) film with the emergence of obvious capacitive reactions on

defective surface, favoring the rapid migrations of sodium ions and solvated compounds, also contribute to the remarkable electrochemical performances of the porous carbon black.

Key Word: Sodium-ion batteries; Anode; Porous carbon; Functionalities; Ether-based electrolyte

1. Introduction

Nowadays, the comprehensively technical penetration of lithium-ion batteries (LIBs) into portable devices tremendously reshaped the modern consumer electronics and primarily propelled the development of electric vehicles as well as the large-scale grid energy storage[1-4]. However, the haunting strategic anxiety concerning the gradual depletion of lithium resources and their geologically restrained distribution challenged the sustainability and the affordability of LIBs in meeting the huge demands of electrical energy storage[5-7]. Sodium-ion batteries (SIBs), inherited the analogous physicochemical properties based on the elemental sodium from the same group in the periodic table as lithium, have emerged as one of the most riveting alternatives for lithium counterparts, due to the ubiquitous sodium resources and the subsequently low cost[8-12]. The intrinsically disadvantageous energy density, resulting from a higher redox potential and a larger atomic weight as well as an increased ionic size, determined the huge potential of SIBs in applications of the large-scale stationary and fluctuating energy storage for the cost-effectiveness [7, 10].

Particularly, the pursuit of advanced electrodes and electrolytes with high rate capabilities and cycle stabilities is the key to enable the high-performance SIBs for the sake of quick response to grid requirement[13]. But the mismatch between a limited interlayer distance for the commercial graphite and a large ionic radius of sodium ion as well as the absence of the thermodynamically stable graphite intercalation compounds[14-17], presented a serious challenge on the selection of a suitable anode substitute. Unfortunately, the sodium metal is severely plagued by the severe safety issues regarding its low melting point and the unavoidable dendrite formation.[6] Initially, disordered carbon materials, which are structurally composed of the curved graphene layers with large interlayer spacings and the turbostratic nanodomains with desirable pores, could generate reversible capacities as high as 300 mAh g^{-1} but with relatively poor rate

capabilities and cycle performances[18-25]. Inspired by lithium equivalents, the rational nanostructured design[26-38] and the appropriate heteroatom doping[34, 39-50], were widely employed to develop carbonaceous materials with a highly reversible capacity and a long cycle life. Simultaneously, the electrochemical performances of carbon-based materials were further promoted by the electrolyte optimization[51-54]. Recently, the layered-structure graphite has been revisited by several groups[55-60]. Philipp Adelhelm and colleagues[55] surprisingly revealed a unique co-intercalation phenomenon of sodium ions and diglyme solvents into graphite by forming a ternary intercalation compound with a highly reversible capacity of 100 mAh g^{-1}. Later, Kisuk Kang et al.[56] further extended this electrochemical behavior to ether-based electrolytes and systematically studied the effects of different solvents/salts on electrochemical properties of natural graphite. According to these findings for ether-based electrolyte, the concept of solvent co-intercalation has been gradually established for sodium ion storage in graphite.[59-68] Additionally, the highly porous carbon materials in ether-based electrolyte could also deliver a large reversible capacity and a long-term cycle life, due to the formation of a uniform and compact solid electrolyte interphase (SEI) layer for the improved structural stability.[64]

In our previous reports, the ether-based electrolyte was found to enable the highly reversible sodiation/desodiation processes for a commercial N330 carbon by efficiently combining the sodium ion insertion into the disordered structure with the solvated sodium ion species co-intercalation into the graphitic structure.[69] Additionally, the desirable microstructure with abundant active sodium storage sites resulted from a NH_3-assisted thermal etching treatment of the pristine carbon blacks can also give rise to a large reversible capacity and ultralong cycle life. As reviewed before[70-71], several critical physicochemical properties involving the interlayer spacing, the porosity, the surface area, the heteroatom doping, and the intercalation behaviors as well as the SEI formation in different electrolytes, would definitely affect the electrochemical performances of carbon-based anode materials for SIBs.

Herein, we firstly developed a surface-functionalized strategy for the porous carbon by a facile CO_2-assisted thermal etching route. With the assistance of an ether-based electrolyte by making most of the active sodium storage sites, the functional groups could greatly boost the migrations of sodium ions/solvated sodium ion species, effectively guarantee the rapid capacitive

reactions on the defective surface, and favorably promote the sodium intercalation/extraction processes, further leading to a superior reversible capacity, an exceptional rate capability, and an outstanding cyclability.

2. Experimental

2.1 Materials synthesis

The commercial N330 carbon black was selected as the pristine material and the introduction of CO_2 at 1050 °C could lead to the formation of the oxygen-containing functional groups for carbon blacks, as elaborated in our previous reports[72-73]. In a typical preparation, 500 mg of pristine carbon black distributed in a fused silica boat was pyrolyzed in a fused silica reactor under CO_2 at 1050 °C until the desired mass losses were obtained. The as-etched samples with the mass loss of 13 wt.%, 30 wt.%, and 50 wt.%, were referred as CBC13, CBC30, and CBC50, respectively. In order to investigate the effects of these oxygen-containing functional groups on electrochemical properties of carbon blacks, as-obtained carbon blacks were further treated under H_2 at 950 °C to effectively remove these oxygen-containing functional groups. The corresponding samples reduced from the as-etched samples with the mass loss of 13%, 30%, and 50%, were denoted as CBCH13, CBCH30, and CBCH50, respectively.

In the preparation of electrolyte, sodium triflate ($NaCF_3SO_3$, 98%, Sigma Aldrich) and molecular sieves (4 Å, Sigma Aldrich) were firstly dried at 150 °C under vacuum for 2 days. The residual water in the commercial solvents was further removed by the as-dried molecular sieves. Finally, the electrolytes using different solvents were carefully obtained in a glove box under Ar atmosphere by dissolving 1.0 M sodium triflate ($NaCF_3SO_3$, 98%, Sigma Aldrich) into diethylene glycol dimethyl ether (DEGDME, 98.9%, Sigma-Aldrich) and ethylene carbonate (EC, 99%, BASF)/diethyl carbonate (DEC, 99%, BASF) with 1:1 in volume ratio (Sigma Aldrich), respectively.

2.2 Physical Characterizations

X-ray Diffraction (XRD) spectroscopy using a Bruker D8Advance (Cu-Kα source, 40kV, 40mA) spectrometer was employed to study the crystalline structures of carbon blacks. Raman scattering spectra were recorded by a HORIBA Scientific LabRAM HR Raman spectrometer

system with a 532.4 nm laser. N_2 adsorption/desorption isotherm and pore size distribution were measured by a Folio Micromeritics Tristar II surface area analyzer. The morphologies of different materials were observed by a Hitachi S-4800 field emission scanning electron microscope (FE-SEM) operated at 5 keV. High resolution transmission electron microscopy (HRTEM) and electron energy-loss spectroscopy (EELS) elemental mapping were conducted by a Gatan GIF-200 spectrometer. For the synchrotron-based X-ray characterizations, O K-edge and C K-edge X-ray absorption spectroscopies (XAS) for different samples were collected in Beamline 6.3.1.2 and 8.0.1.4 of Advanced Light Source in Lawrence Berkeley National Laboratory. The C 1s and O 1s X-ray photoemission spectroscopies (XPS) were conducted at the high resolution Spherical Grating Monochromator (SGM) beamline in Canadian Light Source (CLS). The excitation/pass energy for C 1s and O 1s XPS are 700/20 and 1500/20 eV, respectively.

2.3 Electrochemical measurements

The electrochemical properties of different carbon blacks were measured by examining the typical 2032-type coin cells. For electrode preparation, the slurry, obtained by thoroughly mixing 80 wt.% active carbon materials, 10 wt.% acetylene blacks as the conductive agent, 10 wt.% poly(vinylidene difluoride) (PVDF) binder in a certain amount of N-methyl pyrrolidinone, was then casted onto the copper foil. After dried under vacuum at 80 °C for 12 h, the as-formed electrodes were punched into ½ inch pellets which were further pressed under a certain pressure with the loading mass of about 0.8 mg cm^{-2}. The 2032-type coin cells, which were composed of a sodium foil as anode, a counter electrode as cathode, a polypropylene membrane (Celgard 2400) as separator and electrolytes using different solvents, were assembled in an Argon-filled glove box with the limited moisture and oxygen contents. The galvanotactic charge/discharge tests were performed in the voltage range of 0.001~2.5 V at the different current densities under room temperature by an Arbin BT-2000 Battery Tester. The cyclic voltammetry (CV) measurements were conducted by a versatile multichannel Biologic VMP3 electrochemical station at 0.1 mV s^{-1}, while the electrochemical impedance spectra (EIS) were collected at an AC (alternating current) voltage of 5 mV amplitude in the frequency range of 100 kHz to 0.01 Hz.

3. Results and discussions

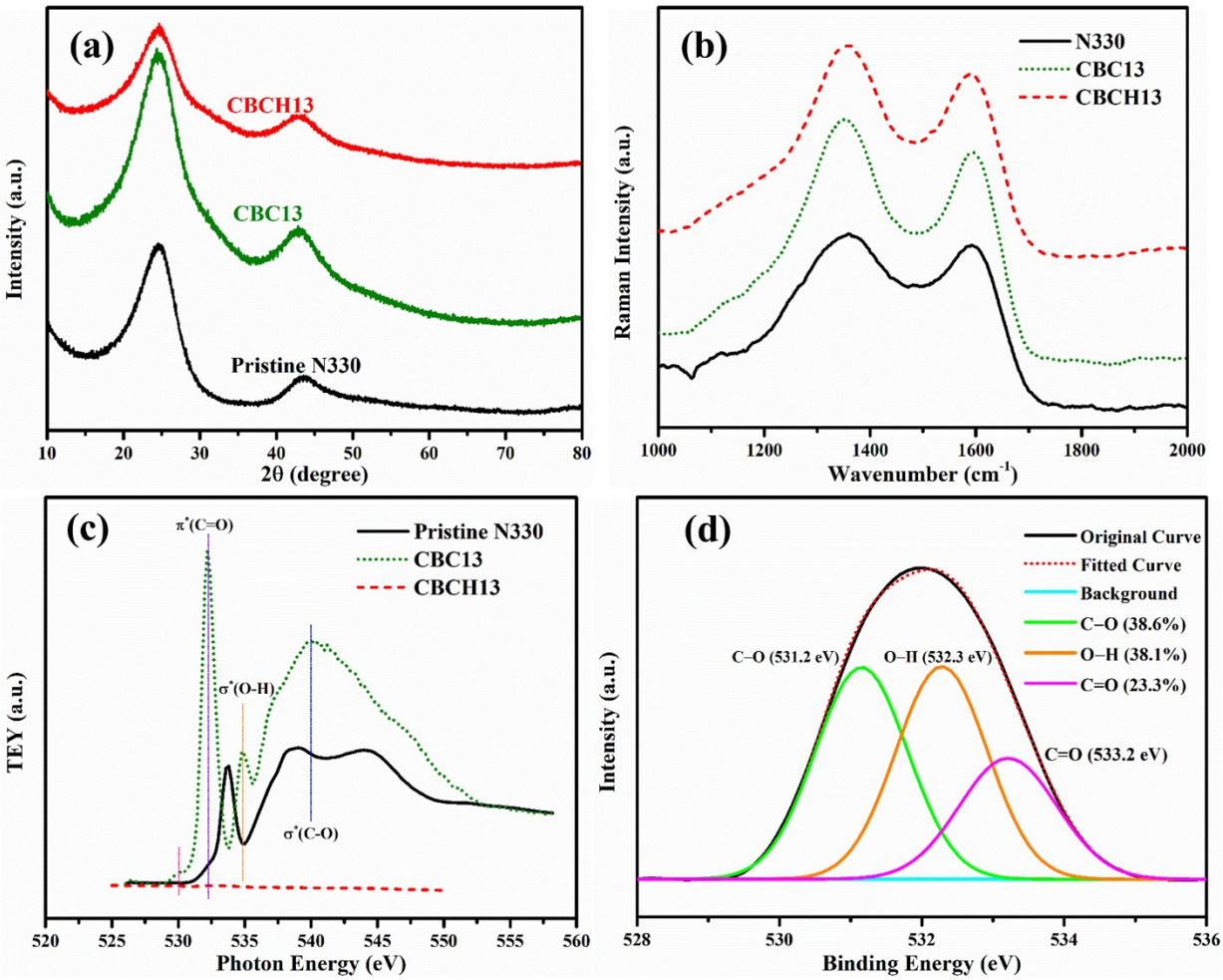

Figure 1 (a) XRD patterns, (b) Raman spectra, and (c) O K-edge X-ray absorption spectroscopies for different carbon blacks. (d) Synchrotron-based O 1s XPS for CBC13 carbon black.

The structural evolutions of different carbon blacks before and after the thermal treatments were studied by XRD and Raman spectra. XRD patterns in Figure 1(a) show two obvious peaks at ~24 ° and ~42°, corresponding to the (002) diffraction plane of layer-by-layer stacking structure for graphene and the (100) diffraction plane of ordered hexagonal structure for graphite, respectively[45, 74]. The coexistence of these two peaks further hints at an amorphous nature of different carbon blacks. According to the Bragg equation and the Scherrer equation[35, 74-75], the interlayer distance (d_{002}), the in-lane coherence length (L_c), and the out-of-lane coherence length (L_a) for the graphitic domains are calculated and listed in Table S1 (Supporting Information). Even though the interlayer distance (d_{002}) almost does not change after different

thermal treatments, the value of L_c apparently increases while the value of L_a obviously decreases, indicating the consumption of amorphous part during the etching process which agrees well with our previous results[72]. Furthermore, the introduction of CO_2 during the thermal treatment could markedly increase the surface area and create the pores with a smaller size. Meanwhile, the disordered (D) band induced from the defects in the disordered structure and the graphitic (G) band resulted from the graphitic structure in crystallite can be identified at 1343 and 1590 cm^{-1} in Raman spectra, respectively [74, 76]. As observed in Figure 1(b), the peak for defect-induced D band obviously sharpens with the decrease of the related half width at half maximum (HWHM) upon the CO_2 etching, while the peak for G band hardly changes, further confirming the decomposition of the disordered part during the CO_2 thermal treatment. It's noteworthy the strange increase of I_D/I_G value after the CO_2 etching process at 1050 °C should be originated from the curling of the stacked graphitic layers with the subsequent shrinkage of the small graphitic crystals in (100) directions[74, 77]. At the same time, the reduced carbon black after annealing in H_2 could present the similar physical properties with a higher surface area and a larger pore size than that of the functionalized carbon black treated in CO_2 (Figure S3-S4). Importantly, the highly surface-sensitive O K-edge X-ray absorption spectroscopies in TEY (Total Electron Yield) mode were conducted to understand the functionalities and the structures of different carbon blacks as shown in Figure 1(c). For pristine N330 carbon black, a strong peak at 533.7 eV can be assigned to the σ* state of C−O from the residual epoxide species, while two broad peaks at 538.5 and 544.0 eV should be ascribed to the σ* C-O transitions from the difference of two C−O bonds in carboxylic acids[78-82]. After the thermal etching in CO_2, CBC13 carbon black could display a weak feature at 530.0 eV and a sharp peak at 532.2 eV, undoubtedly arising from the transitions of O 1s electrons to the π* C=O states[78, 82]. Additionally, an obvious peak at 534.9 eV and a broad peak at 540.0 eV should be derived from the σ* states of O-H and C-O in hydroxyl groups, respectively[79-80, 83-84]. When it comes to the carbon black after the thermal reducing in H_2, no signal can be observed. The evolution of chemical bonds as evidenced in XAS measurements clearly demonstrates the formation of functionalities in carbon black after the annealing process in CO_2 and the effective removal of oxygen-containing functional groups by the subsequent H_2 treatment. Furthermore, a high-resolution synchrotron-based O 1s XPS as depicted in Figure 1(d) was also applied to characterize the chemical states of

oxygen in functionalized carbon. This broad peak could be accordingly deconvoluted into three peaks at 531.2, 532.3, and 533.2 eV, respectively. Two obvious peaks at 531.2 and 533.2 eV should be separately attributed to C–O and C=O bonds in the oxygenated functional groups, while the strong peak at 532.3 eV relates to the O–H bonds in functionalized carbon material[85-90]. Specifically, the proportions of C–O, O–H, and C=O bonds in oxygenated functional groups are estimated to 38.6%, 38.1%, and 23.3%, respectively. At the same time, the corresponding peak in synchrotron-based C 1s XPS for CBC13 carbon black in Figure S2 can also be divided into C–C sp^2, C–C sp^3, C-O, and O=C–O peaks at 284.0, 285.2, 285.6, and 289.2 eV, respectively[91-101]. The rich and cogent information obtained from the underlying structural characterizations and the exceptionally surface-sensitive detections, straightforwardly identified the decomposition of disordered part in carbon structure and the subsequent formation of microporosity as well as functionalities.

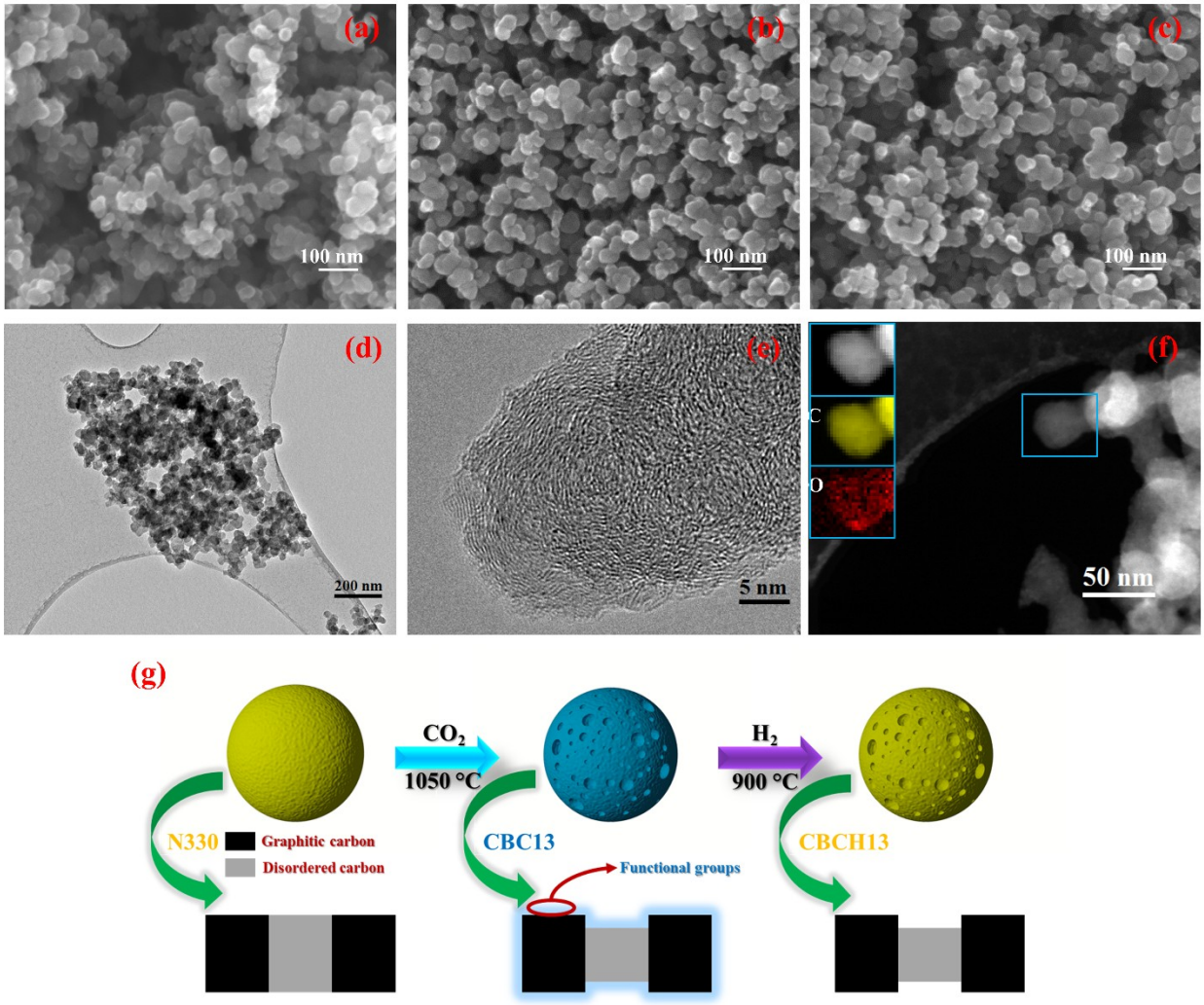

Figure 2 SEM images of (a) N330, (b) CBC13, and (c) CBCH13 carbon blacks. (d) TEM and (e) HRTEM images of CBC13 carbon black. (f) Elemental mappings in EELS for C and O K-edge of CBC13 carbon black. (g) Schematic diagram of the thermal etching and reducing processes.

The morphologies and the structures of different carbon blacks were further examined by SEM and TEM, as displayed in Figure 2(a-f). In the pristine N330 carbon black, the irregular particles with the size ranging from 20 to 60 nm, are unevenly distributed and severely aggregated. After the CO_2 thermal etching process, the tiny particles diminish, and the carbon black exhibits a granular morphology with an average particle size around 50 nm. Moreover, the H_2 thermal reduction could also slightly reduce the particle size without changing the spherical shape of the carbon black. Specifically, an apparent short-range order in turbostratic nanodomains, as shown in HRTEM image of Figure 2(e), reveals an amorphous nature with a

partially graphitic structure for CBC13 carbon black. Additionally, the elemental mappings in EELS at C and O K-edge in Figure 2(f) and Figure S1, critically confirm the intensive formation of the oxygenated functionalities in the surface area of nanoparticles after the CO_2 thermal treatment. Figure 2(g) further illustrates the evolution of carbon black during the CO_2 thermal etching and H_2 thermal reducing processes. Upon reacting with CO_2 at 1050 °C, the disordered part would preferably decompose with the generation of oxygen-containing species on the surface of carbon black. Then these oxygenated groups in the functionalized carbon black could be efficiently removed after the thermal reducing process in H_2 at 900 °C. The presence of oxygenated functionalities will unavoidably affect the processes involving the sodium ion diffusion and the subsequent electrochemical intercalation in carbon materials.

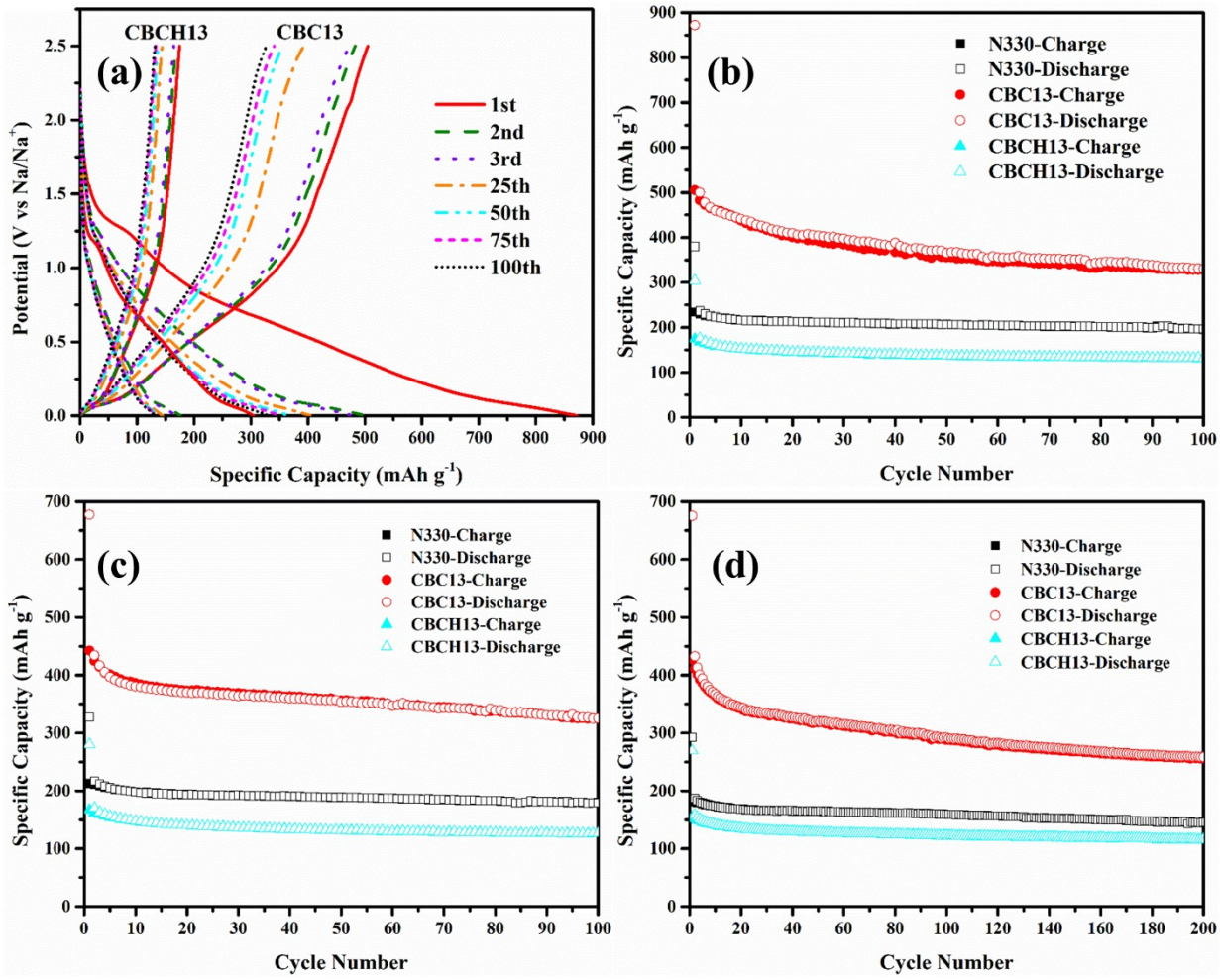

Figure 3 (a) Discharge-charge profiles for CBC13 and CBCH13 carbon black at a current density of 50 mA g^{-1}. Cycle performances of different carbon blacks at current densities of (a) 50, (b) 100, and (c) 200 mA g^{-1}.

The pivotal roles of oxygenated functionalities can be proven by the dramatically different electrochemical performances, as evaluated by the galvanostatic discharge–charge measurements in an ether-based electrolyte for different carbon blacks. In Figure 3(a), the CBC13 carbon black with abundant functional groups delivers an extremely large reversible capacity of 505 mAh g^{-1} with an initial coulombic efficiency of 57.9% at 50 mA g^{-1}, but the thermal reducing process could seriously lower the initial charge capacity for CBCH13 to 175 mAh g^{-1} with a 57.4% coulombic efficiency. Even though the fast capacity fading happens at the beginning of the cycling for CBC13 carbon black, it still exhibits reversible capacities of 483, 472, 393, 356, and 341 mAh g^{-1} at 2nd, 3rd, 25th, 50th, and 75th cycle, respectively, which are much higher than the corresponding results for CBCH13 carbon black. Appealingly, most of the discharged/charged capacities for the functionalized CBC13 carbon black are resulted from the electrochemical intercalation/extraction occurring below 1.5 V, promising its high desirability as an anode material with a high energy density for SIBs. Figure 3(b-d) further compares the cycle performances of different carbon blacks at different current densities. After 100 cycles at 50 mA g^{-1} as shown in Figure 3(b), CBC13 carbon black maintains a reversible capacity of 327 mAh g^{-1} with a 64.8% capacity retention, while N330 and CBCH13 carbon blacks show charge capacities of 196 and 132 mAh g^{-1}, respectively. Admittedly, the rapid capacity decay at first, originated from the slow but complex chemical interactions between the oxygenated functionalities and the electrolytes during the electrochemical reactions, would lead to a comparatively lower value of the capacity retention than these of the pristine N330 and CBCH13 carbon blacks. The oxygen-containing functional groups could greatly facilitate the sodium ion diffusion by abundant ionic/electronic pathways and further enable the subsequent sodiation/desodiation processes by more sodium ion storage sites. When cycled at 100 mA g^{-1} over 100 cycles as shown in Figure 3(c), CBC13 carbon black still shows a high charge capacity of 325 mAh g^{-1} with a 73.5% capacity retention, while the reversible capacities of pristine N330 and CBCH13 carbon blacks stabilize around 180 and 127 mAh g^{-1}, respectively. The superior cycle stability for CBC13

carbon black can also be exemplified in Figure 3(d) with a highly reversible capacity of 256 mAh g^{-1} after 200 cycles at 200 mA g^{-1}, which is much higher than these of the pristine N330 and CBCH13 carbon blacks. Even cycled at 400 and 800 mA g^{-1} over 100 cycles, the reversible capacities of 287 and 278 mAh g^{-1} could still be obtained for CBC13 carbon black, respectively, as displayed in Figure S15. In contrast to the poor electrochemical performances of the pristine N330 and CBCH13 carbon blacks, the significantly improved capacities of CBC13 carbon black, clearly testify the crucial roles of oxygenated functionalities in a highly porous structure, not only facilitating the migrations of electrons/sodium ions through the abundant pathways, but also contributing to the highly efficient sodium ion intercalations/extractions on more active sites. It's necessary to point out both functionalities and porosity have great impacts on the electrochemical properties of carbon blacks, as detailed in Supporting Information.

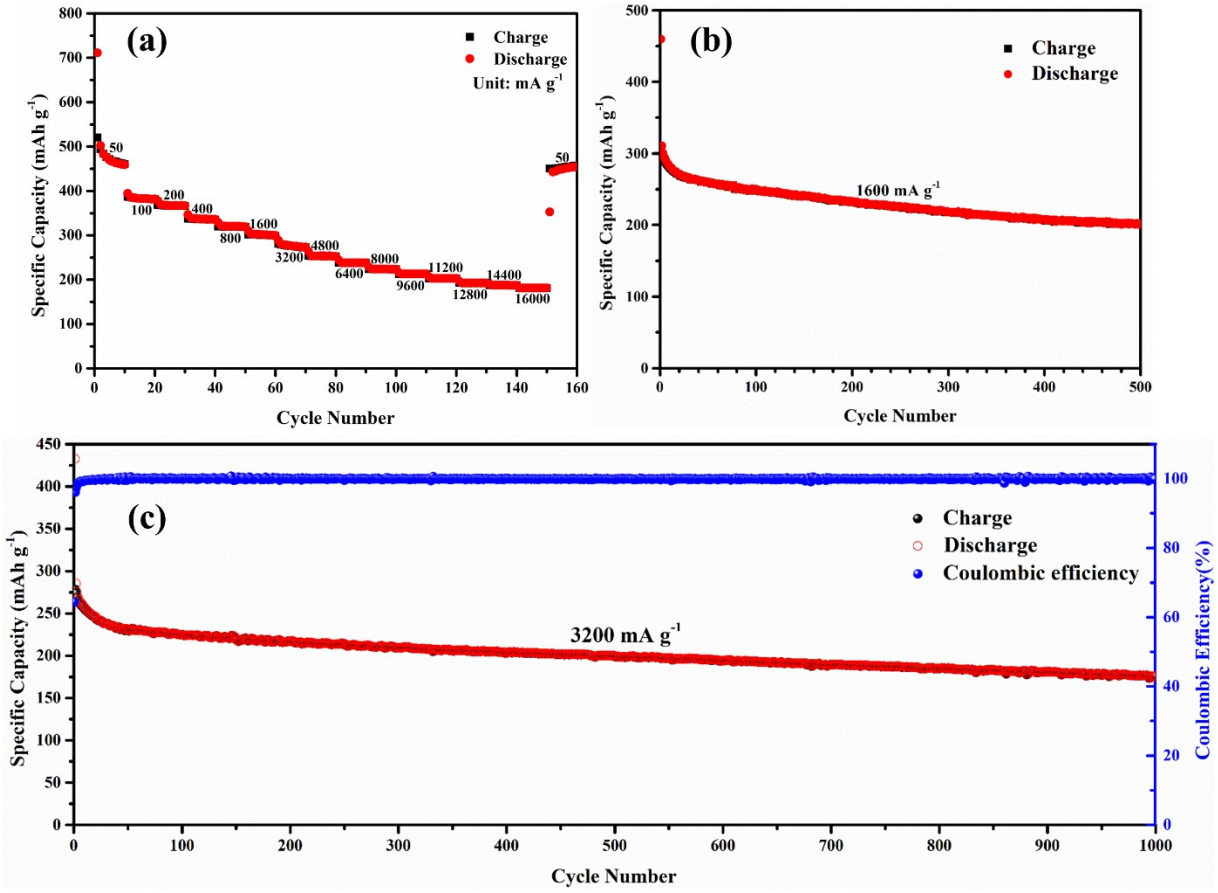

Figure 4 (a) Rate performance at current densities of 50~16000 mA g^{-1}, (b) cycle performance at a current density of 1600 mA g^{-1}, and (c) rate cycle performance at a current density of 3200 mA g^{-1} for CBC13 carbon black.

In addition to the noticeable reversible capacities, the excellent rate capability and the remarkable rate cycle stability can also be recognized for the functionalized carbon black, as shown in Figure 4. When cycled at the current densities of 50, 100, 200, 400, 800, 1600, and 3200 mA g^{-1}, CBC13 carbon black could deliver charge capacities of 471, 383, 366, 336, 319, 300, and 275 mAh g^{-1}, respectively. Simultaneously, this electrode was also able to maintain highly stable capacities of 253, 238, 224, 213, and 203 mAh g^{-1} at the current densities of 4800, 6400, 8000, 9600, and 11200 mA g^{-1}, respectively. Interestingly, the large reversible capacities of 193 and 188 mAh g^{-1} could further achieved for this functionalized electrode at the current densities of 12800 and 14400 mA g^{-1}. Even applied an extremely high current density of 16000 mA g^{-1}, it can still retain a highly reversible capacity of 181 mAh g^{-1} and further regain a large reversible capacity of 453 mAh g^{-1} upon restoring the current density to 50 mA g^{-1}. Impressively, the CBC13 carbon black displays a highly reversible capacity of 202 mAh g^{-1} at 1600 mA g^{-1} over 500 cycles with a 66.44% capacity retention. The outstanding rate cycle performance of 176 mAh g^{-1} with a 0.0369% capacity degradation per cycle and the stable coulombic efficiencies approaching 100% could even be achieved at 3200 mA g^{-1} over 1000 cycles. The superior electrochemical reversibility and exceptional rate cycle capability for the functionalized porous carbon outperform the electrochemical properties of several carbonaceous anodes in recent reports[23-24, 31, 34, 43, 45, 102-109]. The ultrafast sodium ion diffusion and electron transport, benefitted from the oxygenated functional groups in a desirable porous structure with more active sodium ion storage sites, could endow the functionalized carbon black with an ultrahigh rate capability and a highly stable cycle performance.

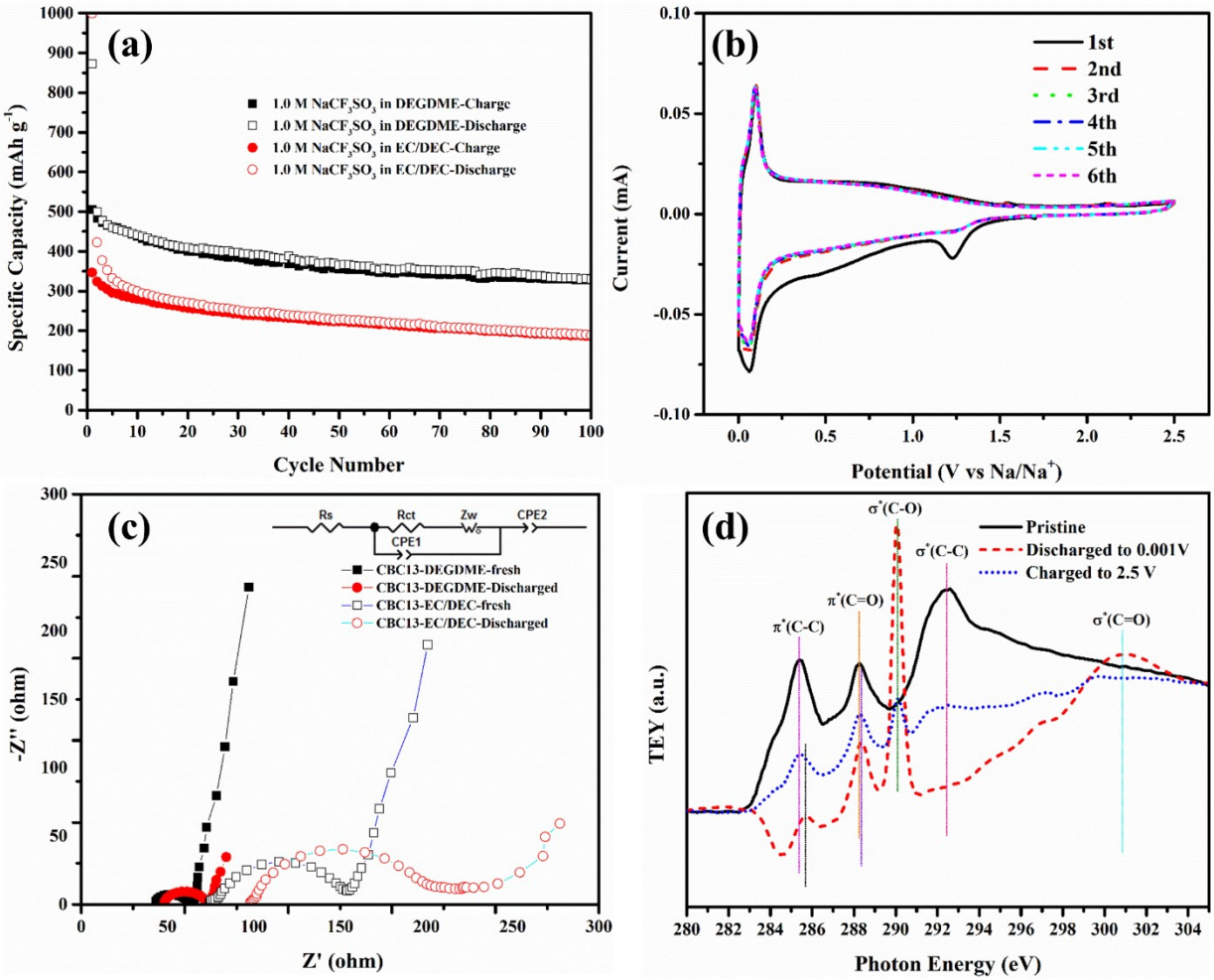

Figure 5 (a) Cycle performances of CBC13 carbon black in different electrolytes using DEGDME and EC/DEC as solvents at a current density of 50 mA g^{-1}. (b) CV curves of CBC13 carbon black in DEGDME-based electrolyte at 0.1 mV s^{-1}. (c) EIS for CBC13 carbon black electrodes before and after discharging in different electrolytes (the inset shows equivalent circuit model). (d) C K-edge X-ray absorption spectroscopies of CBC13 carbon black electrodes at different states when cycling in DEGDME-based electrolyte.

In terms of the carbon anode materials, solvents in electrolytes could also determine the electrochemical sodiation mechanisms and the corresponding electrochemical behaviors[55-57]. In the present case, it is necessary to compare the electrochemical properties of the functionalized carbon black in ether-based and carbonate-based electrolytes to understand the structural evolution of SEI during the discharging/charging processes. In Figure 5(a), CBC13 carbon black

in the EC/DEC-based electrolyte could only present an initial reversible capacity of 347 mAh g^{-1} with a low coulombic efficiency of 34.7% and a poor capacity retention of 53.6% after 100 cycles at 50 mA g^{-1}. The superior electrochemical performance for DEGDME-based electrolyte can also be found in CBCH30 carbon black with an initial reversible capacity of 244 mAh g^{-1} at 50 mA g^{-1} over 100 cycles, as shown in Figure S27. A lower reversible capacity and a faster capacity decay for the carbon black in EC/DEC-based electrolyte should be due to its sole dependence on sodium ion insertion into the disordered structures and uncontrollable accumulations of a thick SEI layer. Comparatively, DEGDME-based electrolyte enables the functionalized porous carbon to fully utilize the potential capacity based on a synergistic combination of the sodium insertion into the disordered structure with the solvated sodium ion species co-intercalation into the graphitic part. Intriguingly, a sharp anodic peak appeared around 0.5 V during the first discharging process for CBC13 carbon black in EC/DEC-based electrolyte in Figure S17, do not arise in the same process for DEGDME-based electrolyte in Figure 5(b), hinting at a distinct SEI formation route for the functionalized carbon black in ether-based electrolyte. At the same time, the negligible differences for intensities and positions of all cathodic/anodic peaks below 0.5 V in the following cycles, further prove the high electrochemical reversibility of the functionalized carbon black. Furthermore, the comparisons of EIS in Figure 5(c) and related parameters in Table S4 for the pristine and discharged electrodes in different electrolytes, also verify the electrochemical advantages of ether-based electrolyte. Owing to the uncontrollable formation of a thick SEI layer on the surface of CBC13 carbon electrode during the discharging process in EC/DEC-based electrolyte, its charge transfer resistance would significantly increase, while the corresponding value in DEGDME-based electrolyte slightly changed. Additionally, the SEI impedance for the discharged electrode in EC/DEC-based electrolyte are much higher than that of DEGDME-based electrolyte, implying the limited formation of a robust and thin SEI film on CBC13 carbon electrode in DEGDME-based electrolyte. On the one hand, the unconstrained generation of a thick SEI layer in EC/DEC-based electrolyte would severely lower the initial reversibility/coulombic efficiency, sacrifice the electrolyte, and inhibit the facile diffusion of sodium ions. On the other hand, the self-limited formation of a robust but thin SEI layer in DEGDME-based electrolyte could effectively stabilize

the carbon structure, accommodate the expanded structure in discharged carbon, and further promote the rapid migration of sodium ions/solvated sodium ion compounds[64, 68].

The formation and evolution of SEI for CBC13 carbon black electrodes in DEGDME-based electrolyte were also investigated by the highly surface-sensitive C K-edge X-ray absorption spectroscopies in TEY (Total Electron Yield) mode, as shown in Figure 5(d). For the pristine CBC13 carbon black, two obvious features at 285.4 and 292.4 eV should correspond to the transitions of C 1s electrons toward the π*(C-C) and σ*(C-C) orbitals[110] , respectively, while the peak at 288.2 eV is related to the π*(C=O) transitions[110-113]. Upon discharging to 0.001 V, the peaks for the π*(C-C) and π*(C=O) transitions shift negatively and the σ*(C-C) feature completely disappears. Importantly, a newly-formed sharp peak around 290.0 eV regarding the σ*(C-O) transitions for the oxygen-containing functional groups[82, 113-114] and a broad peak around 301.0 eV as the σ*(C=O) feature[82, 114-115], can be clearly identified in the XAS measurements, as a strong evidence for the electrolyte decomposition and the subsequent SEI generation. When charged the electrode back to 2.5 V, the π*(C-C) feature moves to the initial position at 285.4 eV and the peak for σ(C-C)* transition reappears around 292.4 eV. Noticeably, the π*(C=O) peak do not change its position as well as intensity while the σ*(C-O) feature still maintains its previous position but with a comparatively lower intensity. The persistence of the σ*(C-O) feature and irreversibility of the π*(C=O) peak elucidate the preservation of a robust SEI thin film, which could not only efficiently facilitate the migration of sodium ions and solvated compounds in electrolyte/interphase/electrode, but also effectively accommodate the volume variations during the cycling and further avoid the overconsumption of electrolyte, leading to a highly reversible capacity and an exceptional rate capability.

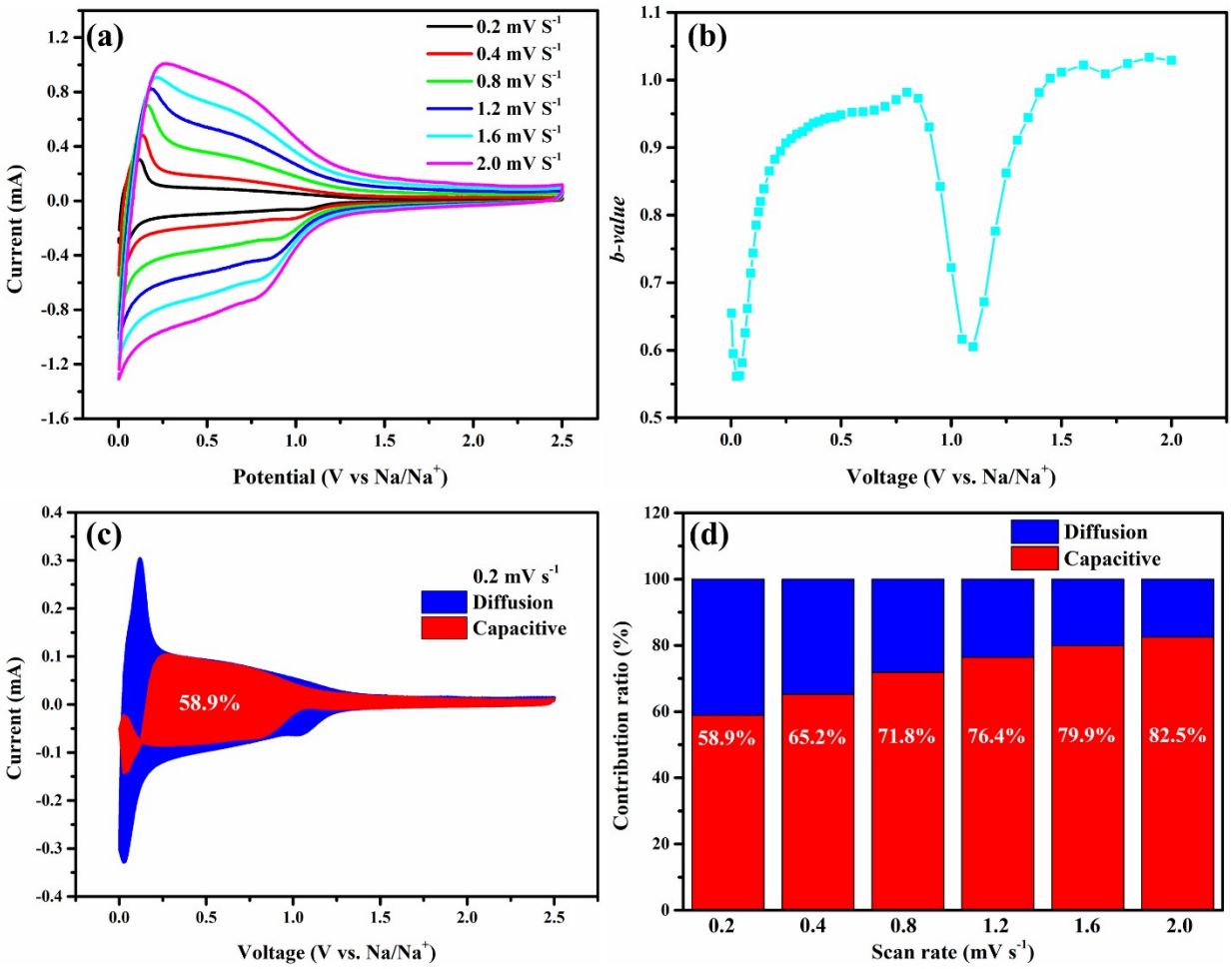

Figure 6 (a) CV curves of CBC13 carbon black at various scan rates. (b) Calculated *b*-values plotted against the battery potentials for CBC13 carbon black in cathodic (sodiation) process. (c) Capacitive contribution at a scan rate of 0.2 mV S^{-1}. (d) Contribution ratios of capacitive capacity at various scan rates.

While the diffusion-controlled intercalations of sodium ions/solvated compounds into graphitic/amorphous structures would primarily determine the electrochemical properties of CBC13 carbon black, the surface-induced capacitive reactions by absorbing these species into cavities/nanopores would also play a vital role in charge storage process of carbon anode materials for SIBs[49, 56, 85, 89, 95, 116-119]. Consequently, the CV measurements at various scan rates in Figure 6(a) were conducted to accurately quantify the diffusive/capacitive contributions and further clarify the sodium storage mechanism during the sodiation/desodiation processes.

Theoretically, the relationship between current response and scan rate can be expressed by a classical power-law formula:

$$i(V)=a\,v^{b} \tag{1}$$

where $i(V)$ (mA) is the absolute value of current response at a specific voltage of V and a corresponding scan rate of v (mV s^{-1}), while a and b are adjustable values. Based on a simple linear fitting of log ($|i(V)|$) versus log(v) plot, the b value can be easily obtained for a specific potential at a certain scan rate. It has been generally recognized that the b value of 0.5 represents a typical diffusion-controlled intercalation reaction, and the b value of 1.0 in a linear relationship of current response with scan rate further corresponds to a capacitance-dominated charge storage. As displayed in Figure 6(b), 50 data points were selected to calculate the b values for CBC13 carbon black at different potentials in the sodiation process between 0.001~2.0 V. Interestingly, the b value would initially approach 1.0 above 1.4 V, then rapidly drop to 0.6 at 1.1 V, subsequently increase to 0.98 at 0.8 V, and finally decreased to 0.59 at 0.01 V, indicating the electrochemical dominances of capacitive reactions at high/medium voltages (>1.4 V and 1.0~0.1 V) and intercalation reactions at relatively low voltages (<0.1 V) with the particular diffusion-controlled reactions around 1.1 V. Simultaneously, the flat CV curves in a rectangular shape at high voltages for various scan rates also prove the leading function of capacitive contribution in sodium storage, while the presence of cathodic/anodic peaks in redox reactions at low voltages further exhibit the dominant role of diffusive contribution in charge storage. Even though the voltage shift for anodic peaks from 0.2 to 2.0 mV s^{-1} could reach a relatively large value of 0.14 V, the cathodic peaks barely changed the voltage position, hinting a low electrochemical polarization and a promising reaction kinetics upon sodiation. On the basis of equation (1), the contribution ratios of capacitive and diffusive reactions can be calculated by the following equation:

$$i(V)=k_1 v+k_2 v^{1/2} \tag{2}$$

where k_1v at a b value of 1.0 represents the capacitive contribution from surface reactions and $k_2v^{1/2}$ at a b value of 0.5 corresponds to the diffusive contribution from intercalation reactions in current response at a specific potential. Though a linear fitting of $i(V)/v^{1/2}$ versus $v^{1/2}$ profile at a

certain potential for different scan rates, the corresponding value of k_1 can be immediately acquired, while various k_1 values could be further plotted against different potentials, resulting in estimated capacitive contributions at various scan rates. When characterized at a scan rate of 0.2 mV s^{-1}, the CBC13 carbon black would deliver a dominating capacitive contribution of 58.9% in Figure 6(c), while the corresponding contribution areas are consistent with the predictions of *b* values. As shown in Figure 6(d) and Figure S20(b-f), this key parameter would continuously increase to 65.2%, 71.8%, 76.4, 79.9%, and 82.5% at scan rates of 0.4, 0.8, 1.2, 1.6, and 2.0 mV s^{-1}, respectively, demonstrating the strong capability of surface oxygenated functionalities to facilitate the rapid migrations of sodium ions/solvated compounds and boost the electrochemical performances of CBC13 carbon black.

With the assistance of an advantageously synergistic mechanism for sodium storage in ether-based electrolyte for carbon anode materials, the oxygenated functionalities could not only generate abundant pathways for migrations of sodium ions/solvated species, but also ensure a fast capacitive reaction on the defective surface, contributing to a large reversible capacity and an excellent rate capability. Meanwhile, the emergence of a robust but thin SEI film and the subsequent preservation would further stabilize the fragile porous structure for the functionalized carbon black. The functionalized porous carbon with a superior cycle performance at exceptionally high rates, are very desirable for applications in grid energy storage with the requirements of a high energy density and a quick response.

4. Conclusion

In summary, the functionalized porous carbon black derived from a CO_2 thermal etching route was successfully applied as an anode material for SIBs. Benefitted from its abundant oxygenated functionalities and the desirable microporosity with the obvious pseudocapacitive behaviors, the etched carbon black could deliver an extremely large reversible capacity (505 mAh g^{-1} at 50 mA g^{-1}), an outstanding cycle stability (176 mAh g^{-1} at 3200 mA g^{-1} after 1000 cycles), and an exceptional rate capability (126 mAh g^{-1} at 12800 mA g^{-1}). As unearthed by the electrochemical and physiochemical characterizations, the controllable formation and the subsequent preservation of a robust but thin SEI film in the electrochemical reactions, could not only facilitate the migrations of sodium ions and solvated compounds, but also stabilize the

fragile structure for porous carbon materials upon the sodium ion intercalation/extraction processes. At the same time, the surface-induced capacitive reactions on the defective surface would further contribute to the charge storage process upon sodiation. The novelty of oxygenated functionalities on the promotion of sodium storage capability and the advantage of ether-based electrolytes for a controllable generation of a SEI thin film, have directly opened a new avenue for developing high-performance carbon anode materials for SIBs.

Acknowledgements

This research was supported by the Natural Science and Engineering Research Council of Canada (NSERC), the Canada Research Chair Program (CRC), the Canada Foundation for Innovation (CFI), and the University of Western Ontario (UWO). Dr. Jian Liu is grateful to the financial support from NSERC Postdoctoral Fellowships Program. This research used resources of the Advanced Light Source, which is a DOE Office of Science User Facility under contract no. DE-AC02-05CH11231.

References

(1) Armand, M.; Tarascon, J.-M. Building better batteries. *Nature* **2008,** *451*, 652-657, DOI: 10.1038/451652a.
(2) Larcher, D.; Tarascon, J.-M. Towards greener and more sustainable batteries for electrical energy storage. *Nat. Chem.* **2015,** *7*, 19-29, DOI: 10.1038/nchem.2085.
(3) Tarascon, J. M. Key challenges in future Li-battery research. *Phil. Trans. R. Soc. A* **2010,** *368* (1923), 3227-3241, DOI: 10.1098/rsta.2010.0112.
(4) Tarascon, J.-M.; Armand, M. Issues and challenges facing rechargeable lithium batteries. *Nature* **2001,** *6861* (414), 359-367, DOI: 10.1038/35104644.
(5) Ellis, B. L.; Nazar, L. F. Sodium and sodium-ion energy storage batteries. *Curr. Opin. Solid State Mater. Sci.* **2012,** *16* (4), 168-177, DOI: 10.1016/j.cossms.2012.04.002.
(6) Slater, M. D.; Kim, D.; Lee, E.; Johnson, C. S. Sodium-Ion Batteries. *Adv. Funct. Mater.* **2013,** *23* (8), 947-958, DOI: 10.1002/adfm.201200691.
(7) Palomares, V.; Serras, P.; Villaluenga, I.; Hueso, K. B.; Carretero-González, J.; Rojo, T. Na-ion batteries, recent advances and present challenges to become low cost energy storage systems. *Energy Environ. Sci.* **2012,** *5* (3), 5884-5901, DOI: 10.1039/c2ee02781j.
(8) Yabuuchi, N.; Kubota, K.; Dahbi, M.; Komaba, S. Research development on sodium-ion batteries. *Chem. Rev.* **2014,** *114* (23), 11636-82, DOI: 10.1021/cr500192f.
(9) Kundu, D.; Talaie, E.; Duffort, V.; Nazar, L. F. The emerging chemistry of sodium ion batteries for electrochemical energy storage. *Angew. Chem. Int. Ed.* **2015,** *54* (11), 3431-3448, DOI: 10.1002/anie.201410376.

(10) Pan, H.; Hu, Y.-S.; Chen, L. Room-temperature stationary sodium-ion batteries for large-scale electric energy storage. *Energy Environ. Sci.* **2013,** *6* (8), 2338-2360, DOI: 10.1039/c3ee40847g.
(11) Fang, Y.; Xiao, L.; Chen, Z.; Ai, X.; Cao, Y.; Yang, H. Recent Advances in Sodium-Ion Battery Materials. *Electrochem. Energ. Rev.* **2018,** *1* (3), 294-323, DOI: 10.1007/s41918-018-0008-x.
(12) Wang, T.; Su, D.; Shanmukaraj, D.; Rojo, T.; Armand, M.; Wang, G. Electrode Materials for Sodium-Ion Batteries: Considerations on Crystal Structures and Sodium Storage Mechanisms. *Electrochem. Energ. Rev.* **2018,** *1* (2), 200-237, DOI: 10.1007/s41918-018-0009-9.
(13) Yang, Z.; Zhang, J.; Kintner-Meyer, M. C.; Lu, X.; Choi, D.; Lemmon, J. P.; Liu, J. Electrochemical energy storage for green grid. *Chem. Rev.* **2011,** *111* (5), 3577-613, DOI: 10.1021/cr100290v.
(14) Asher, R. C. A lamellar compound of sodium and graphite. *J. Inorg. Nucl. Chem.* **1959,** *10*, 238-249, DOI: 10.1038/181409a0.
(15) DiVincenzo, D. P.; Mele, E. J. Self-consistent effective-mass theory for intralayer screening in graphite intercalation compounds. *Phys. Rev. B* **1984,** *29* (4), 1685-1694, DOI: 10.1103/PhysRevB.29.1685.
(16) Ge, P.; Fouletier, M. Electrochemical intercalation of sodium in graphite. *Solid State Ionics* **1988,** *28-30*, 1172-1175, DOI: 10.1016/0167-2738(88)90351-7.
(17) Doeff, M. M.; Ma, Y.; Visco, S. J.; Jonghe, L. C. D. Electrochemical Insertion of Sodium into Carbon. *J. Electrochem. Soc.* **1993,** *140*, L169-L170, DOI: 10.1149/1.2221153.
(18) Stevens, D. A.; Dahn, J. R. High Capacity Anode Materials for Rechargeable Sodium Ion Batteries. *J. Electrochem. Soc.* **2000,** *147* (4), 1271-1273, DOI: 10.1149/1.1393348.
(19) Thomas, P.; Billaud, D. Electrochemical insertion of sodium into hard carbons. *Electrochim. Acta* **2002,** *47*, 3303-3307, DOI: 10.1016/S0013-4686(02)00250-5.
(20) Alcántara, R.; Madrigal, F. J. F.; Lavela, P.; Tirado, J. L.; Mateos, J. M. J.; Salazar, C. G. d.; Stoyanova, R.; Zhecheva, E. Characterisation of mesocarbon microbeads (MCMB) as active electrode material in lithium and sodium cells. *Carbon* **2001,** *38* (7), 1031-1041, DOI: 10.1016/S0008-6223(99)00215-8.
(21) Alcántara, R.; Jiménez Mateos, J. M.; Tirado, J. L. Negative Electrodes for Lithium- and Sodium-Ion Batteries Obtained by Heat-Treatment of Petroleum Cokes below 1000°C. *J. Electrochem. Soc.* **2002,** *149* (2), A201-A205, DOI: 10.1149/1.1431963.
(22) Alcántara, R.; Jiménez-Mateos, J. M.; Lavela, P.; Tirado, J. L. Carbon black-a promising electrode material for sodium-ion batteries. *Electrochem. Commun.* **2001,** *3* (11), 639-642, DOI: 10.1016/S1388-2481(01)00244-2.
(23) Li, Y.; Hu, Y.-S.; Qi, X.; Rong, X.; Li, H.; Huang, X.; Chen, L. Advanced sodium-ion batteries using superior low cost pyrolyzed anthracite anode: towards practical applications. *Energy storage mater.* **2016,** *5*, 191-197, DOI: 10.1016/j.ensm.2016.07.006.
(24) Liu, P.; Li, Y.; Hu, Y.-S.; Li, H.; Chen, L.; Huang, X. A waste biomass derived hard carbon as a high-performance anode material for sodium-ion batteries. *J. Mater. Chem. A* **2016,** *4* (34), 13046-13052, DOI: 10.1039/c6ta04877c.
(25) Bai, P.; He, Y.; Zou, X.; Zhao, X.; Xiong, P.; Xu, Y. Elucidation of the Sodium-Storage Mechanism in Hard Carbons. *Adv. Energy Mater.* **2018**, 1703217, DOI: 10.1002/aenm.201703217.

(26) Wenzel, S.; Hara, T.; Janek, J.; Adelhelm, P. Room-temperature sodium-ion batteries: Improving the rate capability of carbon anode materials by templating strategies. *Energy Environ. Sci.* **2011,** *4* (9), 3342-3345, DOI: 10.1039/c1ee01744f.
(27) Tang, K.; Fu, L.; White, R. J.; Yu, L.; Titirici, M.-M.; Antonietti, M.; Maier, J. Hollow Carbon Nanospheres with Superior Rate Capability for Sodium-Based Batteries. *Adv. Energy. Mater.* **2012,** *2* (7), 873-877, DOI: 10.1002/aenm.201100691.
(28) Cao, Y.; Xiao, L.; Sushko, M. L.; Wang, W.; Schwenzer, B.; Xiao, J.; Nie, Z.; Saraf, L. V.; Yang, Z.; Liu, J. Sodium ion insertion in hollow carbon nanowires for battery applications. *Nano Lett.* **2012,** *12* (7), 3783-3787, DOI: 10.1021/nl3016957.
(29) Chen, T.; Liu, Y.; Pan, L.; Lu, T.; Yao, Y.; Sun, Z.; Chu, D. H. C.; Chen, Q. Electrospun carbon nanofibers as anode material for sodium ion batteries with excellent cycle performance. *J. Mater. Chem. A* **2014,** *2*, 4117-4121, DOI: 10.1039/C3TA14806H.
(30) Luo, W.; Schardt, J.; Bommier, C.; Wang, B.; Razink, J.; Simonsen, J.; Ji, X. Carbon nanofibers derived from cellulose nanofibers as a long-life anode material for rechargeable sodium-ion batteries. *J. Mater. Chem. A* **2013,** *1* (36), 10662-10666, DOI: 10.1039/c3ta12389h.
(31) Li, Y.; Hu, Y.-S.; Titirici, M.-M.; Chen, L.; Huang, X. Hard Carbon Microtubes Made from Renewable Cotton as High-Performance Anode Material for Sodium-Ion Batteries. *Adv. Energy Mater.* **2016**, 1600659, DOI: 10.1002/aenm.201600659.
(32) Wang, Y.-X.; Chou, S.-L.; Liu, H.-K.; Dou, S.-X. Reduced graphene oxide with superior cycling stability and rate capability for sodium storage. *Carbon* **2013,** *57*, 202-208, DOI: 10.1016/j.carbon.2013.01.064.
(33) Wang, Y.; Wang, C.; Wang, Y.; Liu, H.; Huang, Z. Boric Acid Assisted Reduction of Graphene Oxide: A Promising Material for Sodium-Ion Batteries. *ACS Appl. Mater. Interfaces* **2016,** *8* (29), 18860-6, DOI: 10.1021/acsami.6b04774.
(34) Yang, J.; Zhou, X.; Wu, D.; Zhao, X.; Zhou, Z. S-Doped N-Rich Carbon Nanosheets with Expanded Interlayer Distance as Anode Materials for Sodium-Ion Batteries. *Adv. Mater.* **2017,** *29* (6), DOI: 10.1002/adma.201604108.
(35) Ding, J.; Wang, H.; Li, Z.; Kohandehghan, A.; Cui, K.; Xu, Z.; Zahiri, B.; Tan, X.; Lotfabad, E. M.; Olsen, B. C.; Mitlin, D. Carbon Nanosheet Frameworks Derived from Peat Moss as High Performance Sodium Ion Battery Anodes. *ACS Nano* **2013,** *7* (12), 11004-11015, DOI: 10.1021/nn404640c.
(36) Hou, H.; Banks, C. E.; Jing, M.; Zhang, Y.; Ji, X. Carbon Quantum Dots and Their Derivative 3D Porous Carbon Frameworks for Sodium-Ion Batteries with Ultralong Cycle Life. *Adv. Mater.* **2015,** *27*, 7861-7866, DOI: 10.1002/adma.201503816.
(37) Wang, M.; Yang, Z.; Li, W.; Gu, L.; Yu, Y. Superior Sodium Storage in 3D Interconnected Nitrogen and Oxygen Dual-Doped Carbon Network. *Small* **2016,** *12* (19), 2529, DOI: 10.1002/smll.201600101.
(38) Cho, S. Y.; Kang, M.; Choi, J.; Lee, M. E.; Yoon, H. J.; Kim, H. J.; Leal, C.; Lee, S.; Jin, H.-J.; Yun, Y. S. Pyrolytic Carbon Nanosheets for Ultrafast and Ultrastable Sodium-Ion Storage. *Small* **2018,** *14* (17), 1703043, DOI: 10.1002/smll.201703043.
(39) Li, D.; Zhang, L.; Chen, H.; Ding, L.-x.; Wang, S.; Wang, H. Nitrogen-doped bamboo-like carbon nanotubes: promising anode materials for sodium-ion batteries. *Chem. Commun.* **2015,** *51*, 16045-16048, DOI: 10.1039/C5CC06266G.
(40) Xu, J.; Wang, M.; Wickramaratne, N. P.; Jaroniec, M.; Dou, S.; Dai, L. High-Performance Sodium Ion Batteries Based on Three-Dimensional Anode from Nitrogen-Doped Graphene Foams. *Adv. Mater.* **2015,** *27* (12), 2042-2048, DOI: 10.1002/adma.201405370.

(41) Yang, F.; Zhang, Z.; Du, K.; Zhao, X.; Chen, W.; Lai, Y.; Li, J. Dopamine derived nitrogen-doped carbon sheets as anode materials for high-performance sodium ion batteries. *Carbon* **2015,** *91*, 88-95, DOI: 10.1016/j.carbon.2015.04.049.
(42) Li, W.; Zhou, M.; Li, H.; Wang, K.; Cheng, S.; Jiang, K. A high performance sulfur-doped disordered carbon anode for sodium ion batteries. *Energy Environ. Sci.* **2015,** *8*, 2916-2921, DOI: 10.1039/c5ee01985k.
(43) Zhang, S.; Yao, F.; Yang, L.; Zhang, F.; Xu, S. Sulfur-doped mesoporous carbon from surfactant-intercalated layered double hydroxide precursor as high-performance anode nanomaterials for both Li-ion and Na-ion batteries. *Carbon* **2015,** *93*, 143-150, DOI: 10.1016/j.carbon.2015.04.091.
(44) Wang, P.; Qiao, B.; Du, Y.; Li, Y.; Zhou, X.; Dai, Z.; Bao, J. Fluorine-Doped Carbon Particles Derived from Lotus Petioles as High-Performance Anode Materials for Sodium-Ion Batteries. *J. Phys. Chem. C* **2015,** *119* (37), 21336-21344, DOI: 10.1021/acs.jpcc.5b05443.
(45) Yoon, D.; Kim, D. H.; Chung, K. Y.; Chang, W.; Kim, S. M.; Kim, J. Hydrogen-enriched porous carbon nanosheets with high sodium storage capacity. *Carbon* **2016,** *98*, 213-220, DOI: 10.1016/j.carbon.2015.11.009.
(46) Wang, X.; Li, G.; Hassan, F. M.; Li, J.; Fan, X.; Batmaz, R.; Xiao, X.; Chen, Z. Sulfur covalently bonded graphene with large capacity and high rate for high-performance sodium-ion batteries anodes. *Nano Energy* **2015,** *15*, 746-754, DOI: 10.1016/j.nanoen.2015.05.038.
(47) Liu, H.; Jia, M.; Cao, B.; Chen, R.; Lv, X.; Tang, R.; Wu, F.; Xu, B. Nitrogen-doped carbon/graphene hybrid anode material for sodium-ion batteries with excellent rate capability. *J. Power Sources* **2016,** *319*, 195-201, DOI: 10.1016/j.jpowsour.2016.04.040.
(48) Yan, D.; Yu, C.; Zhang, X.; Qin, W.; Lu, T.; Hu, B.; Li, H.; Pan, L. Nitrogen-doped carbon microspheres derived from oatmeal as high capacity and superior long life anode material for sodium ion battery. *Electrochem. Acta* **2016,** *191*, 385-391, DOI: 10.1016/j.electacta.2016.01.105.
(49) Qian, J.; Wu, F.; Ye, Y.; Zhang, M.; Huang, Y.; Xing, Y.; Qu, W.; Li Li; Chen, R. Boosting Fast Sodium Storage of a Large-Scalable Carbon Anode with an Ultralong Cycle Life. *Adv. Energy Mater.* **2018**, 1703159, DOI: 10.1002/aenm.201703159.
(50) Li, Y.; Yuan, Y.; Bai, Y.; Liu, Y.; Wang, Z.; Limin Li; Wu, F.; Amine, K.; Wu, C.; Lu, J. Insights into the Na^+ Storage Mechanism of Phosphorus-Functionalized Hard Carbon as Ultrahigh Capacity Anodes. *Adv. Energy Mater.* **2018**, 1702781, DOI: 10.1002/aenm.201702781.
(51) Komaba, S.; Murata, W.; Ishikawa, T.; Yabuuchi, N.; Ozeki, T.; Nakayama, T.; Ogata, A.; Gotoh, K.; Fujiwara, K. Electrochemical Na Insertion and Solid Electrolyte Interphase for Hard-Carbon Electrodes and Application to Na-Ion Batteries. *Adv. Funct. Mater.* **2011,** *21* (20), 3859-3867, DOI: 10.1002/adfm.201100854.
(52) Ponrouch, A.; Marchante, E.; Courty, M.; Tarascon, J.-M.; Palacín, M. R. In search of an optimized electrolyte for Na-ion batteries. *Energy Environ. Sci.* **2012,** *5* (9), 8572, DOI: 10.1039/c2ee22258b.
(53) Ponrouch, A.; Goñi, A. R.; Palacín, M. R. High capacity hard carbon anodes for sodium ion batteries in additive free electrolyte. *Electrochem. Commun.* **2013,** *27*, 85-88, DOI: 10.1016/j.elecom.2012.10.038.
(54) Ponrouch, A.; Dedryvère, R.; Monti, D.; Demet, A. E.; Ateba Mba, J. M.; Croguennec, L.; Masquelier, C.; Johansson, P.; Palacín, M. R. Towards high energy density sodium ion batteries through electrolyte optimization. *Energy Environ. Sci.* **2013,** *6* (8), 2361-2369, DOI: 10.1039/c3ee41379a.

(55) Jache, B.; Adelhelm, P. Use of Graphite as a Highly Reversible Electrode with Superior Cycle Life for Sodium-Ion Batteries by Making Use of Co-Intercalation Phenomena. *Angew. Chem. Int. Ed.* **2014,** *53*, 10169-10173, DOI: 10.1002/anie.201403734.
(56) Kim, H.; Hong, J.; Park, Y.-U.; Kim, J.; Hwang, I.; Kang, K. Sodium Storage Behavior in Natural Graphite using Ether-based Electrolyte Systems. *Adv. Funct. Mater.* **2014,** *25* (4), 534-541, DOI: 10.1002/adfm.201402984.
(57) Kim, H.; Hong, J.; Yoon, G.; Kim, H.; Park, K.-Y.; Park, M.-S.; Yoon, W.-S.; Kang, K. Sodium intercalation chemistry in graphite. *Energy Environ. Sci.* **2015,** *8*, 2963-2969, DOI: 10.1039/c5ee02051d.
(58) Wen, Y.; He, K.; Zhu, Y.; Han, F.; Xu, Y.; Matsuda, I.; Ishii, Y.; Cumings, J.; Wang, C. Expanded graphite as superior anode for sodium-ion batteries. *Nat. Commun.* **2014,** *5*, 4033, DOI: 10.1038/ncomms5033.
(59) Zhu, Z.; Cheng, F.; Hu, Z.; Niu, Z.; Chen, J. Highly stable and ultrafast electrode reaction of graphite for sodium ion batteries. *J. Power Sources* **2015,** *293*, 626-634, DOI: 10.1016/j.jpowsour.2015.05.116.
(60) Gotoh, K.; Maruyama, H.; Miyatou, T.; Mizuno, M.; Urita, K.; Ishida, H. Structure and Dynamic Behavior of Sodium–Diglyme Complex in the Graphite Anode of Sodium Ion Battery by 2H Nuclear Magnetic Resonance. *J. Phys. Chem. C* **2016,** *120* (49), 28152-28156, DOI: 10.1021/acs.jpcc.6b10962.
(61) Jung, S. C.; Kang, Y.-J.; Han, Y.-K. Origin of excellent rate and cycle performance of Na^+-solvent cointercalated graphite vs. poor performance of Li^+-solvent case. *Nano Energy* **2017,** *34*, 456-462, DOI: 10.1016/j.nanoen.2017.03.015.
(62) Zhu, Y.-E.; Yang, L.; Zhou, X.; Li, F.; Wei, J.; Zhou, Z. Boosting the rate capability of hard carbon with an ether-based electrolyte for sodium ion batteries. *J. Mater. Chem. A* **2017,** *5* (20), 9528-9532, DOI: 10.1039/c7ta02515g.
(63) L. Seidl; Bucher, N.; Chu, E.; Hartung, S.; Martens, S.; Schneider, O.; Stimming, U. Intercalation of solvated Na-ions into graphite. *Energy Environ. Sci.* **2017,** *10*, 1631-1642, DOI: 10.1039/C7EE00546F.
(64) Zhang, J.; Wang, D.-W.; Lv, W.; Zhang, S.; Liang, Q.; Zheng, D.; Kang, F.; Yan, Q.-H. Achieving superb sodium storage performance on carbon anodes through an ether-derived solid electrolyte interphase. *Energy Environ. Sci.* **2017,** *10*, 370-376, DOI: 10.1039/c6ee03367a.
(65) Jache, B.; Binder, J. O.; Abe, T.; Adelhelm, P. A comparative study on the impact of different glymes and their derivatives as electrolyte solvents for graphite co-intercalation electrodes in lithium-ion and sodium-ion batteries. *Phys. Chem. Chem. Phys.* **2016,** *18* (21), 14299-316, DOI: 10.1039/c6cp00651e.
(66) Guan, Z.; Shen, X.; Yu, R.; Wang, Z.; Chen, L. Chemical intercalation of solvated sodium ions in graphite. *Electrochim. Acta* **2016,** *222*, 1365-1370, DOI: 10.1016/j.electacta.2016.11.112.
(67) Hasa, I.; Dou, X.; Buchholz, D.; Shao-Horn, Y.; Hassoun, J.; Passerini, S.; Scrosati, B. A sodium-ion battery exploiting layered oxide cathode, graphite anode and glyme-based electrolyte. *J. Power Sources* **2016,** *310*, 26-31, DOI: 10.1016/j.jpowsour.2016.01.082.
(68) Goktas, M.; Bolli, C.; Berg, E. J.; Novák, P.; Kilian Pollok; Langenhorst, F.; Roeder, M. v.; Lenchuk, O.; Mollenhauer, D.; Adelhelm, P. Graphite as Cointercalation Electrode for Sodium-Ion Batteries: Electrode Dynamics and the Missing Solid Electrolyte Interphase (SEI). *Adv. Energy Mater.* **2018**, 1702724, DOI: 10.1002/aenm.201702724.

(69) Xiao, W.; Sun, Q.; Liu, J.; Xiao, B.; Glans, P.-A.; Li, J.; Li, R.; Guo, J.; Yang, W.; Sham, T.-K.; Sun, X. Utilizing the full capacity of carbon black as anode for Na-ion batteries via solvent co-intercalation. *Nano Res.* **2017,** *10* (12), 4378-4387, DOI: 10.1007/s12274-017-1852-4.
(70) Bommier, C.; Ji, X. Recent Development on Anodes for Na-Ion Batteries. *Isr. J. Chem.* **2015,** *55* (5), 486-507, DOI: 10.1002/ijch.201400118.
(71) Balogun, M.-S.; Luo, Y.; Qiu, W.; Liu, P.; Tong, Y. A review of carbon materials and their composites with alloy metals for sodium ion battery anodes. *Carbon* **2016,** *98*, 162-178, DOI: 10.1016/j.carbon.2015.09.091.
(72) Li, Y.; Li, X.; Geng, D.; Tang, Y.; Li, R.; Dodelet, J.-P.; Lefèvre, M.; Sun, X. Carbon black cathodes for lithium oxygen batteries: Influence of porosity and heteroatom-doping. *Carbon* **2013,** *64*, 170-177, DOI: 10.1016/j.carbon.2013.07.049.
(73) Li, X.; Li, X.; Banis, M. N.; Wang, B.; Lushington, A.; Cui, X.; Li, R.; Sham, T.-K.; Sun, X. Tailoring interactions of carbon and sulfur in Li–S battery cathodes: significant effects of carbon–heteroatom bonds. *J. Mater. Chem. A* **2014,** *2* (32), 12866, DOI: 10.1039/c4ta02007c.
(74) Li, Y.; Hu, Y.-S.; Li, H.; Chen, L.; Huang, X. A superior low-cost amorphous carbon anode made from pitch and lignin for sodium-ion batteries. *J. Mater. Chem. A* **2015,** *4* (1), 96-104, DOI: 10.1039/C5TA08601A.
(75) Biscoe, J. An X-Ray Study of Carbon Black. *J. Appl. Phys.* **1942,** *13* (6), 364, DOI: 10.1063/1.1714879.
(76) Lv, W.; Zhao, J.; Wen, F.; Xiang, J.; Li, L.; Wang, L.; Liu, Z.; Tian, Y. Carbonaceous photonic crystals as ultralong cycling anodes for lithium and sodium batteries. *J. Mater. Chem. A* **2015,** *3*, 13786-13793, DOI: 10.1039/C5TA02873F.
(77) Li, Y.; Mu, L.; Hu, Y.-S.; Li, H.; Chen, L.; Huang, X. Pitch-derived amorphous carbon as high performance anode for sodium-ion batteries. *Energy storage mater.* **2016,** *2*, 139-145, DOI: 10.1016/j.ensm.2015.10.003i.
(78) Zhang, Z.; Pfefferle, L.; Haller, G. L. Comparing characterization of functionalized multi-walled carbon nanotubes by potentiometric proton titration, NEXAFS, and XPS. *Chinese J. Catal.* **2014,** *35*, 856-863, DOI: 10.1016/S1872-2067(14)60123-6.
(79) Jeong, H. K.; Noh, H. J.; Kim, J. Y.; Jin, M. H.; Park, C. Y.; Lee, Y. H. X-ray absorption spectroscopy of graphite oxide. *EPL (Europhysics Letters)* **2008,** *82* (6), 67004, DOI: 10.1209/0295-5075/82/67004.
(80) Lee, V.; Whittaker, L.; Jaye, C.; Baroudi, K. M.; Fischer, D. A.; Banerjee, S. Large-Area Chemically Modified Graphene Films: Electrophoretic Deposition and Characterization by Soft X-ray Absorption Spectroscopy. *Chem. Mater.* **2009,** *21* (16), 3905-3916, DOI: 10.1021/cm901554p.
(81) Smith, J. W.; Lam, R. K.; Sheardy, A. T.; Shih, O.; Rizzuto, A. M.; Borodin, O.; Harris, S. J.; Prendergast, D.; Saykally, R. J. X-Ray absorption spectroscopy of $LiBF_4$ in propylene carbonate: a model lithium ion battery electrolyte. *Phys. Chem. Chem. Phys.* **2014,** *16*, 23568-23575, DOI: 10.1039/c4cp03240c.
(82) Banerjee, S.; Hemraj-Benny, T.; Balasubramanian, M.; Fischer, D. A.; Misewich, J. A.; Wong, S. S. Ozonized single-walled carbon nanotubes investigated using NEXAFS spectroscopy. *Chem. Commun.* **2004,** *0* (7), 772-773, DOI: 10.1039/b315390h.
(83) Francis, J. T.; Hitchcock, A. P. Inner-Shell Spectroscopy of p-Benzoquinone, Hydroquinone, and Phenol- Distinguishing Quilold and Benzenold Structures. *J. Phys. Chem.* **1992,** *96*, 6598-6610, DOI: 10.1021/j100195a018.

(84) Näslund, L.-Å.; Lüning, J.; Ufuktepe, Y.; Ogasawara, H.; Wernet, P.; Bergmann, U.; Pettersson, L. G. M.; Nilsson, A. X-ray Absorption Spectroscopy Measurements of Liquid Water. *J. PHys. Chem. B* **2005,** *109* (28), 13835-13839, DOI: 10.1021/jp052046q.
(85) Luo, D.; Xu, J.; Guo, Q.; Fang, L.; Zhu, X.; Xia, Q.; Xia, H. Surface-Dominated Sodium Storage Towards High Capacity and Ultrastable Anode Material for Sodium-Ion Batteries. *Adv. Funct. Mater.* **2018,** *28* (47), 1805371, DOI: 10.1002/adfm.201805371.
(86) Javed, M.; Saqib, A. N. S.; Ata-ur-Rehman; Ali, B.; Faizan, M.; Anang, D. A.; Iqbal, Z.; Abbas, S. M. Carbon quantum dots from glucose oxidation as a highly competent anode material for lithium and sodium-ion batteries. *Electrochem. Acta* **2019,** *297*, 250-257, DOI: 10.1016/j.electacta.2018.11.167.
(87) He, Y.; Bai, P.; Gao, S.; Xu, Y. Marriage of an Ether-Based Electrolyte with Hard Carbon Anodes Creates Superior Sodium-Ion Batteries with High Mass Loading. *ACS Appl. Mater. Interfaces* **2018,** *10* (48), 41380-41388, DOI: 10.1021/acsami.8b15274.
(88) Guo, Y.; Liu, W.; Wu, R.; Sun, L.; Zhang, Y.; Cui, Y.; Liu, S.; Wang, H.; Shan, B. Marine-Biomass-Derived Porous Carbon Sheets with a Tunable N-Doping Content for Superior Sodium-Ion Storage. *ACS Appl. Mater. Interfaces* **2018,** *10* (44), DOI: 10.1021/acsami.8b14304.
(89) Huang, M.; Xi, B.; Feng, Z.; Liu, J.; Feng, J.; Qian, Y.; Xiong, S. Facile synthesis of N,O-codoped hard carbon on the kilogram scale for fast capacitive sodium storage. *J. Mater. Chem. A* **2018,** *6* (34), 16465-16474 DOI: 10.1039/C8TA06160B
(90) Thangavel, R.; Kannan, A. G.; Ponraj, R.; Sun, X.; Kim, D.-W.; Lee, Y.-S. Highly interconnected hollow graphene nanospheres as an advanced high energy and high power cathode for sodium metal batteries *J. Mater. Chem. A* **2018,** *6* (21), 9846-9853 DOI: 10.1039/C8TA00153G.
(91) Chai, L.; Wang, J.; Wang, H.; Zhang, L.; Yu, W.; Mai, L. Porous carbonized graphene-embedded fungus film as an interlayer for superior Li–S batteries. *Nano Energy* **2015,** *17*, 224-232, DOI: 10.1016/j.nanoen.2015.09.001.
(92) Haerle, R.; Riedo, E.; Pasquarello, A.; Baldereschi, A. sp2/sp3 hybridization ratio in amorphous carbon from C1scоre-level shifts: X-ray photoelectron spectroscopy and first-principles calculation. *Phys. Rev. B* **2001,** *65* (4), DOI: 10.1103/PhysRevB.65.045101.
(93) Yan, J.; Wei, T.; Shao, B.; Ma, F.; Fan, Z.; Zhang, M.; Zheng, C.; Shang, Y.; Qian, W.; Wei, F. Electrochemical properties of graphene nanosheet/carbon black composites as electrodes for supercapacitors. *Carbon* **2010,** *48* (6), 1731-1737, DOI: 10.1016/j.carbon.2010.01.014.
(94) Yuan, D.; Yuan, X.; Zou, W.; Zeng, F.; Huang, X.; Zhou, S. Synthesis of graphitic mesoporous carbon from sucrose as a catalyst support for ethanol electro-oxidation. *J. Mater. Chem.* **2012,** *22* (34), 17820, DOI: 10.1039/c2jm33658h.
(95) Chen, W.; Chen, C.; Xiong, X.; Hu, P.; Hao, Z.; Huang, Y. Coordination of Surface-Induced Reaction and Intercalation: Toward a High-Performance Carbon Anode for Sodium-Ion Batteries. *Adv. Sci.* **2017,** *4* (6), 1600500, DOI: 10.1002/advs.201600500.
(96) Lü, H.-Y.; Zhang, X.-H.; Wan, F.; Liu, D.-S.; Fan, C.-Y.; Xu, H.-M.; Wang, G.; Wu, X.-L. Flexible P-Doped Carbon Cloth: Vacuum-Sealed Preparation and Enhanced Na-Storage Properties as Binder-Free Anode for Sodium Ion Batteries. *ACS Appl. Mater. Interfaces* **2017,** *9* (14), 12518-12527, DOI: 10.1021/acsami.7b01986.
(97) Hou, H.; Shao, L.; Zhang, Y.; Zou, G.; Chen, J.; Ji, X. Large-Area Carbon Nanosheets Doped with Phosphorus: A High-Performance Anode Material for

Sodium-Ion Batteries. *Adv. Sci.* **2017,** *4* (1), 1600243, DOI: 10.1002/advs.201600243.
(98) Zhang, Y.; Meng, Y.; Wang, Y.; Chen, L.; Guo, Y.; Xiao, D. Sodium Carboxymethylcellulose Derived Oxygen-Rich Porous Carbon Anodes for High-Performance Lithium/Sodium-Ion Batteries. *ChemElectroChem* **2017,** *4* (3), 500-507, DOI: 10.1002/celc.201600577.
(99) Liu, S.; Zhou, J.; Song, H. 2D Zn-Hexamine Coordination Frameworks and Their Derived N-Rich Porous Carbon Nanosheets for Ultrafast Sodium Storage. *Adv. Energy Mater.* **2018,** *8* (22), 1800569, DOI: 10.1002/aenm.201800569.
(100) Shi, W.; Zhang, Y.; Tian, Z. Q.; Pan, Z.; Key, J.; Shen, P. K. Low temperature synthesis of polyhedral hollow porous carbon with high rate capability and long-term cycling stability as Li-ion and Na-ion battery anode material. *J. Power Sources* **2018,** *398*, 149-158, DOI: 10.1016/j.jpowsour.2018.07.038.
(101) Li, W.; Wang, K.; Cheng, S.; Jiang, K. Self-polymerized disordered carbon with interlayer bonded by sulfur atoms enabling high sodium storage performance. *ChemElectroChem* **2018,** *5* (21), 3206-3212, DOI: 10.1002/celc.201800962.
(102) Xiao, L.; Cao, Y.; Henderson, W. A.; Sushko, M. L.; Shao, Y.; Xiao, J.; Wang, W.; Engelhard, M. H.; Nie, Z.; Liu, J. Hard Carbon Nanoparticles as High-capacity, High-stability Anodic Materials for Na-ion Batteries. *Nano Energy* **2016,** *19*, 279-288, DOI: 10.1016/j.nanoen.2015.10.034.
(103) Li, S.; Qiu, J.; Lai, C.; Ling, M.; Zhao, H.; Zhang, S. Surface capacitive contributions: Towards high rate anode materials for sodium ion batteries. *Nano Energy* **2015,** *12*, 224-230, DOI: 10.1016/j.nanoen.2014.12.032.
(104) Bai, Y.; Wang, Z.; Wu, C.; Xu, R.; Wu, F.; Liu, Y.; Li, H.; Li, Y.; Lu, J.; Amine, K. Hard Carbon Originated from Polyvinyl Chloride Nanofibers as High Performance Anode Material for Na-ion Battery. *ACS Appl. Mater. Interfaces* **2015,** *7* (9), 5598-5604, DOI: 10.1021/acsami.5b00861.
(105) Jo, C.; Park, Y.; Jeong, J.; Lee, K. T.; Lee, J. Structural Effect on Electrochemical Performance of Ordered Porous Carbon Electrodes for Na-Ion Batteries. *ACS Appl. Mater. Interfaces* **2015,** *7* (22), 11748-11754, DOI: 10.1021/acsami.5b03186.
(106) Xu, D.; Chen, C.; Xie, J.; Zhang, B.; Miao, L.; Cai, J.; Huang, Y.; Zhang, L. A Hierarchical N/S-Codoped Carbon Anode Fabricated Facilely from Cellulose/Polyaniline Microspheres for High-Performance Sodium-Ion Batteries. *Adv. Energy Mater.* **2016,** *6* (16), 1501929, DOI: 10.1002/aenm.201501929.
(107) Gaddam, R. R.; Yang, D.; Narayan, R.; Raju, K.; Kumar, N. A.; Zhao, X. S. Biomass derived carbon nanoparticle as anodes for high performance sodium and lithium ion batteries. *Nano Energy* **2016,** *26*, 346-352, DOI: 10.1016/j.nanoen.2016.05.047.
(108) Deng, X.; Xie, K.; Li, L.; Zhou, W.; Sunarso, J.; Shao, Z. Scalable synthesis of self-standing sulfur-doped flexible graphene films as recyclable anode materials for low-cost sodium-ion batteries. *Carbon* **2016,** *107*, 67-73, DOI: 10.1016/j.carbon.2016.05.052.
(109) Wen, Y.; Wang, B.; Luo, B.; Wang, L. Long-Term Cycling Performance of Nitrogen-Doped Hollow Carbon Nanospheres as Anode Materials for Sodium-Ion Batteries. *Eur. J. Inorg. Chem.* **2016,** *2016* (13-14), 2051-2055, DOI: 10.1002/ejic.201501172.
(110) Zhou, J.; Zhou, X.; Li, R.; Sun, X.; Ding, Z.; Cutler, J.; Sham, T.-K. Electronic structure and luminescence center of blue luminescent carbon nanocrystals. *Chem. Phys. Lett.* **2009,** *474* (4-6), 320-324, DOI: 10.1016/j.cplett.2009.04.075.

(111) Zhou, J.; Zhou, X.; Sun, X.; Li, R.; Murphy, M.; Ding, Z.; Sun, X.; Sham, T.-K. Interaction between Pt nanoparticles and carbon nanotubes – An X-ray absorption near edge structures (XANES) study. *Chem. Phys. Lett.* **2007,** *437* (4-6), 229-232, DOI: 10.1016/j.cplett.2007.02.026.
(112) Bouchet-Fabre, B.; Pinault, M.; Pichot, V.; Launois, P.; Mayne-L'Hermite, M.; Parent, P.; Laffon, K.; Durand, D.; Reynaud, C. NEXAFS and X-ray scattering study of structure changes after post-annealing treatments of aligned MWNTs. *Diamond Relat. Mater.* **2005,** *14* (3-7), 881-886, DOI: 10.1016/j.diamond.2004.11.018.
(113) Roy, S. S.; Papakonstantinou, P.; Okpalugo, T. I. T.; Murphy, H. Temperature dependent evolution of the local electronic structure of atmospheric plasma treated carbon nanotubes: Near edge X-ray absorption fine structure study. *J. Appl. Phys.* **2006,** *100* (5), 053703, DOI: 10.1063/1.2260821.
(114) Kuznetsova, A.; Popova, I.; John T. Yates, J.; Bronikowski, M. J.; Huffman, C. B.; Liu, J.; Smalley, R. E.; Hwu, H. H.; Chen, J. G. Oxygen-Containing Functional Groups on Single-Wall Carbon Nanotubes: NEXAFS and Vibrational Spectroscopic Studies. *J. Am. Chem. Soc.* **2001,** *123* (43), 10699-10704, DOI: 10.1021/ja011021b.
(115) Nyberg, M.; Hasselström, J.; Karis, O.; Wassdahl, N.; Weinelt, M.; Nilsson, A.; Pettersson, L. G. M. The electronic structure and surface chemistry of glycine adsorbed on Cu(110). *J. Chem. Phys.* **2000,** *112* (12), 5420-5427, DOI: 10.1063/1.481110.
(116) Yao, X.; Ke, Y.; Ren, W.; Wang, X.; Xiong, F.; Yang, W.; Qin, M.; Li, Q.; Mai, L. Defect-Rich Soft Carbon Porous Nanosheets for Fast and High-Capacity Sodium-Ion Storage. *Adv. Energy Mater.* **2019,** *9* (6), 1803260, DOI: 10.1002/aenm.201803260
(117) Yang, H.; Xua, R.; Yu, Y. A facile strategy toward sodium-ion batteries with ultra-long cycle life and high initial Coulombic Efficiency: Free-standing porous carbon nanofiber film derived from bacterial cellulose. *Energy Storage Mater.* **2019,** *22*, 105-112, DOI: 10.1016/j.ensm.2019.01.003.
(118) Liu, L.; Chen, Y.; Xie, Y.; Tao, P.; Wang, Z.; Li, Q.; Wang, K.; Yan, C. Enhanced Interfacial Kinetics of Carbon Monolith Boosting Ultrafast Na-Storage. *Small* **2019,** *15* (5), 1804158, DOI: 10.1002/smll.201804158
(119) Hu, X.; Sun, X.; Yoo, S. J.; Evanko, B.; Fan, F.; Cai, S.; Zheng, C.; Hu, W.; Stucky, G. D. Nitrogen-rich hierarchically porous carbon as a high-rate anode material with ultra-stable cyclability and high capacity for capacitive sodium-ion batteries. *Nano Energy* **2019,** *56*, 828-839, DOI: 10.1016/j.nanoen.2018.11.081.